ORIGINAL ARTICLE

Analysis of the equivalent plastic displacement influence on chip morphology during the orthogonal cutting process using CEL modeling

Mark Vargas[1] · Edgar Isaac Ramírez[1] · Osvaldo Ruiz[1] · Carlos Reyes-Ruiz[2] · Armando Ortiz[1]

Abstract

Machining is one of the more widely used manufacturing processes in the industry, for this reason, several studies have focused on predicting the effect of variables related to it. In this work, the effect of the equivalent plastic displacement on the orthogonal cutting process, using coupled Lagrangian–Eulerian (CEL) analysis was studied. The workpiece was considered Eulerian solid material to simulate its interaction with the cutting tool and thus, predict material separation and chip morphology. In the present model, the chip morphology was evaluated in terms of the equivalent plastic displacement, segmented chip formation was achieved without the necessity to apply a method of mesh separation and undeleting elements during the calculation solution, which represents an important advantage over the purely Lagrangian method. Additionally, the cutting forces, contact length, angle of the cutting plane, as well as stress, strain, and temperature distribution were obtained.

Keywords Orthogonal cutting · Chip morphology · Finite element modeling · CEL analysis

1 Introduction

Variables prediction such as temperature, cutting forces, and stress distribution, play an important role in the optimization of cutting parameters and tools design. These variables have been determined using experimental techniques involving long and expensive processes; hence, the finite element method (FEM) has become an important tool to predict material behavior. According to Özel and Davim [1] it is possible to establish a classification depending on the model description, based on the finite element method to simulate a cutting process: Lagrangian, Eulerian, arbitrary Lagrangian–Eulerian (ALE), and extended arbitrary Lagrangian–Eulerian finite element modeling (X-ALE-FEM). In a Lagrangian analysis, the mesh is distorted as long as material deformation, while in an Eulerian analysis,

the mesh is fixed in space. The Lagrangian formulation has been used mainly to study the current process [2–4]; this requires remeshing techniques to achieve material flow simulation around the tool during cutting, through elements deletion when failure criterion is reached, crack generation and chip formation are simulated [5]. The ALE technique combines the characteristics of a Lagrangian and Eulerian analysis and avoids remeshing for models where large deformations are required; for this reason, it is suitable for orthogonal cutting processes [1, 6]. On the other hand, it has been established that modeling chip morphology depends on some parameters such as friction coefficient, damage parameters, cutting speed, cutting depth, and feed, among others [7–11]. A precise chip morphology is important because it states the cutting process stability, and it helps in well understanding and improving machined surface integrity [12]. A new computational technique has been presented, based on the extended finite element method (X-ALE-FEM) in large plasticity deformations[13] and plasticity forming of powder compaction [14]. An ALE technique is employed to capture the advantages of both Lagrangian and Eulerian methods and alleviate the drawbacks of the mesh distortion in the Lagrangian formulation. In order to remove the limitation of the mesh conforming to the boundary conditions in the simulation, the X-FEM

✉ Carlos Reyes-Ruiz
 c.reyesruiz@unam.mx

1 Departamento de Diseño Y Manufactura, Facultad de Ingeniería, Universidad Nacional Autónoma de México, Cd. Universitaria, 04510 Coyoacán, Mexico

2 Departamento de Diseño Y Manufactura, Facultad de Ingeniería, Universidad Nacional Autónoma de México, PIIT, 66629 Apodaca, Mexico
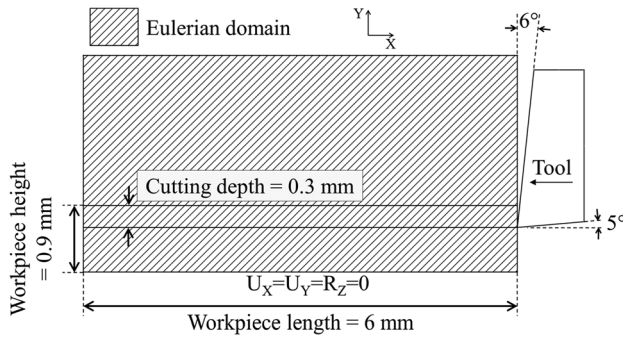
Fig. 1 Orthogonal cutting configuration, Eulerian domain, and tool assembly

Table 2 Thermal and mechanical properties of AISI 1045 steel [25]

Density $\rho[kg/m^3]$	Young modulus $E[GPa]$	Poisson ratio ν	Specific heat $C_p[JKg^{-1}\,{}^\circ C]^{-1}]$	Conductivity $\lambda[W/m\,{}^\circ C]$
7800	200	0.3	474	55

was implemented by incorporating discontinuous fields through a partition of unity method. In order to demonstrate the efficiency of the X-ALE-FEM technique in large deformations, several numerical examples were presented, and the results were compared with those of classical FE and X-FEMs [15].

This study uses the CEL (coupled Eulerian–Lagrangian) method available in ABAQUS®, to provide an alternative solution to the excessive deformation mesh problem where damage criterion, energy, and a standard Coulomb model are sufficient [12, 16] and do not require a criterion of mesh separation and elements deletion to simulate chip formation [17–20]. The conventional Johnson–Cook damage parameters for an AISI 1045 steel and damage evolution were specified in terms of the equivalent plastic displacement. Hence, the objective of this paper is to correlate the equivalent plastic displacement with chip morphology during the orthogonal cutting process to provide a framework focused on understanding the orthogonal cutting process and correlating modeling parameters to improve simulation results.

2 Modeling methodology

The workpiece was considered a deformable Eulerian 3D solid and cutting tool as a deformable 3D solid restricted as a rigid body, with a thickness of 2 mm. Model geometry and assembly are shown in Fig. 1, cutting depth and cut length were 0.3 mm, and 3 mm, respectively, reproducing the operating conditions used by Artozoul et al. [21]. As boundary conditions, the workpiece base and left side were encastre; all the model was restricted in a z-direction (perpendicular

direction to the plane presented in Fig. 1). Then, the Eulerian domain is divided into two regions: the one associated with the workpiece height with the material assignment and the upper region as an empty mesh; during the simulation, it is the region where the chip will grow during the material movement throughout the Eulerian mesh.

The Johnson–Cook model is shown in Eq. (1); it was used to calculate the thermomechanical behavior of an AISI 1045 steel; the values considered are shown in Table 1. Thermal and mechanical values related to a 1045 steel are presented in Table 2.

$$\sigma_{eq} = \left(A + B\epsilon_p{}^n\right)\left(1 + C\mathrm{Ln}\left(\frac{\dot{\epsilon}_p}{\dot{\epsilon}_p^0}\right)\right)\left(1 - \frac{T - T_r}{T_m - T_r}\right)^m \quad (1)$$

where ϵ_p is equivalent strain, $\dot{\epsilon}_p^0$ is reference strain rate ($\dot{\epsilon}_p^0 = 0.001s^{-1}$), T is absolute temperature, T_r is room temperature, T_m is metal melt temperature, and A, B, C, n, and m are material constants [22, 23].

To achieve the characteristic segmented chip geometry, it was used a failure criterion for the Johnson–Cook plasticity model, which is suitable only for high strain rates of metals. The failure model is based on the equivalent plastic strain value in the element integration points. It is assumed that failure occurs when damage parameter D, presented in Eq. (2), exceeds 1.

$$D = \sum\left[\frac{\Delta\bar{\epsilon}^{pl}}{\bar{\epsilon}_f^{pl}}\right] \quad (2)$$

where $\Delta\bar{\epsilon}^{pl}$ is an increase in equivalent plastic strain at failure, $\bar{\epsilon}_f^{pl}$, which is assumed to be dependent on the deformation ratio $\dot{\bar{\epsilon}}^{pl}/\dot{\epsilon}_0$, the ratio p/q, where p is hydrostatic pressure, and q is Von Mises stress, temperature $\hat{\theta}$, which is defined on the Johnson–Cook model, and damage parameters, which are experimentally determined. It was assumed that these relationships are separable, as is shown in Eq. (3) [26].

Table 1 Constants of the Johnson–Cook model for AISI 1045 steel [24]

$A[MPa]$	$B[MPa]$	n	C	m	$\dot{\epsilon}_0[s^{-1}]$	$T_m[{}^\circ C]$	$T_0[{}^\circ C]$
553	600	0.234	0.0134	1.0	0.001	1460	20

Table 3 Damage parameters of the Johnson–Cook model for AISI 1045 steel [27]

d_1	d_2	d_3	d_4	d_5
0.05	4.42	− 2.73	0.0018	0.55

$$\bar{\varepsilon}_f^{pl} = \left(d_1 + d_2\exp\left(d_3\frac{p}{q}\right)\right)\left(1 + d_4\mathrm{Ln}\left(\frac{\dot{\bar{\varepsilon}}^{pl}}{\dot{\varepsilon}_0}\right)\right)\left(1 + d_5\,\hat{\theta}\right) \tag{3}$$

The damage parameters for an AISI 1045 steel are shown in Table 3.

When material damage occurs, the stress–strain relationship no longer accurately represents the material's behavior, then damage evolution was specified in terms of the equivalent plastic displacement $\bar{u}^{pl}$ or fracture dissipation energy G_f. The implementation of the stress-displacement concept in a finite element model requires the characteristic length definition of the element L, associated with an integration point. Fracture energy was defined by Eq. (4).

Table 4 $\bar{u}^{\mathbf{pl}}$ values for 4 models

	$\bar{u}^{\mathbf{pl}}$
Model 1	No failure criterion
Model 2	400
Model 3	50
Model 4	25

$$G_f = \int_{\bar{\varepsilon}_0^{pl}}^{\bar{\varepsilon}_f^{pl}} L\sigma_y d\bar{\varepsilon}^{pl} = \int_0^{\bar{u}_f^{pl}} \sigma_y d\bar{u}^{pl} \tag{4}$$

The evolution of the damage variable with the equivalent plastic displacement can be specified in tabular, linear, or exponential form. Instantaneous failure will occur if the plastic displacement failure is specified as 0, but it is not recommended because it causes a sudden drop in stress and can lead to dynamic instabilities.

In model 1, no failure criterion was used. In model 2, model 3, and model 4, a failure criterion was included to analyze its effect on the chip generation. Table 4 summarizes $\bar{u}^{\mathbf{pl}}$ values used for different models.
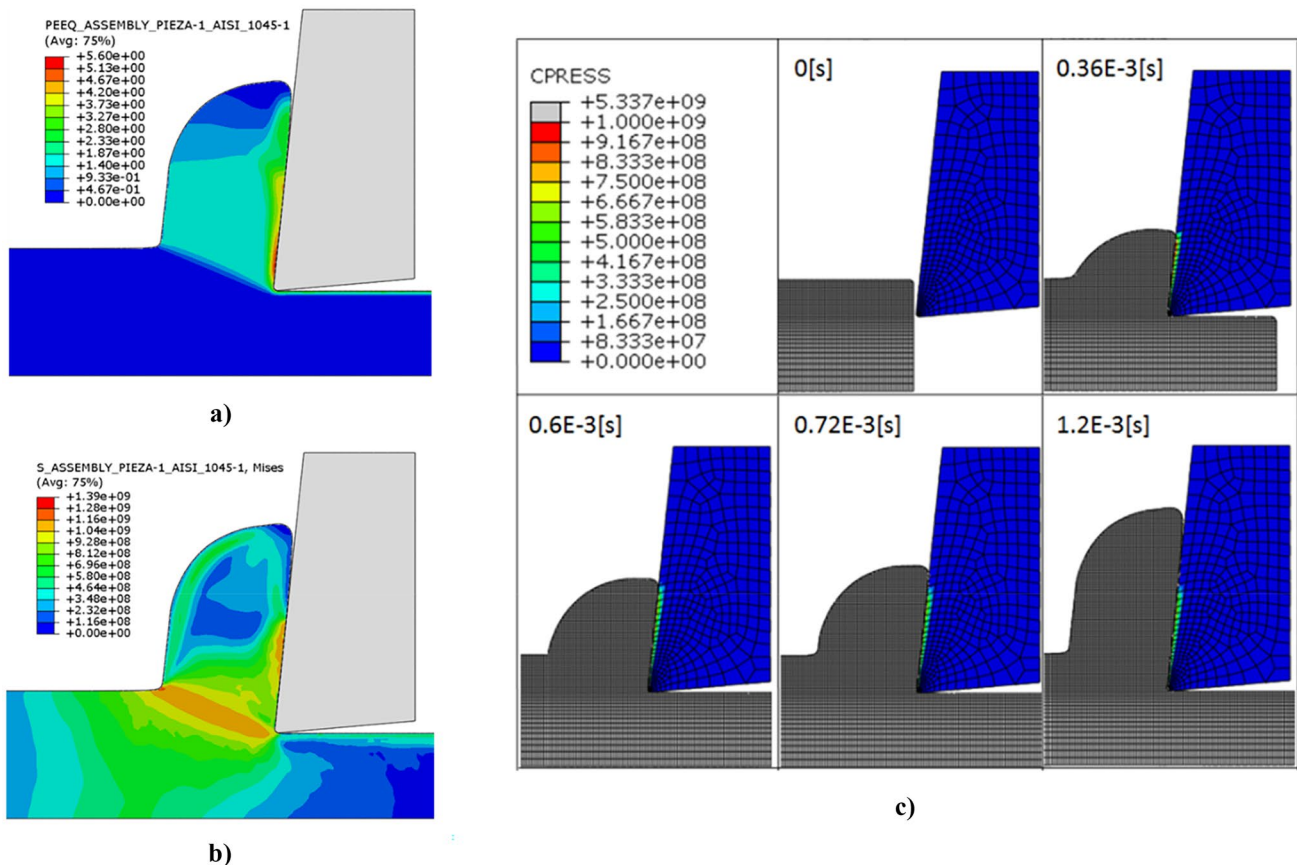

Fig. 2 **a** Equivalent plastic strain, **b** Von Mises stresses [Pa], and **c** contact pressure during chip formation (model 1).
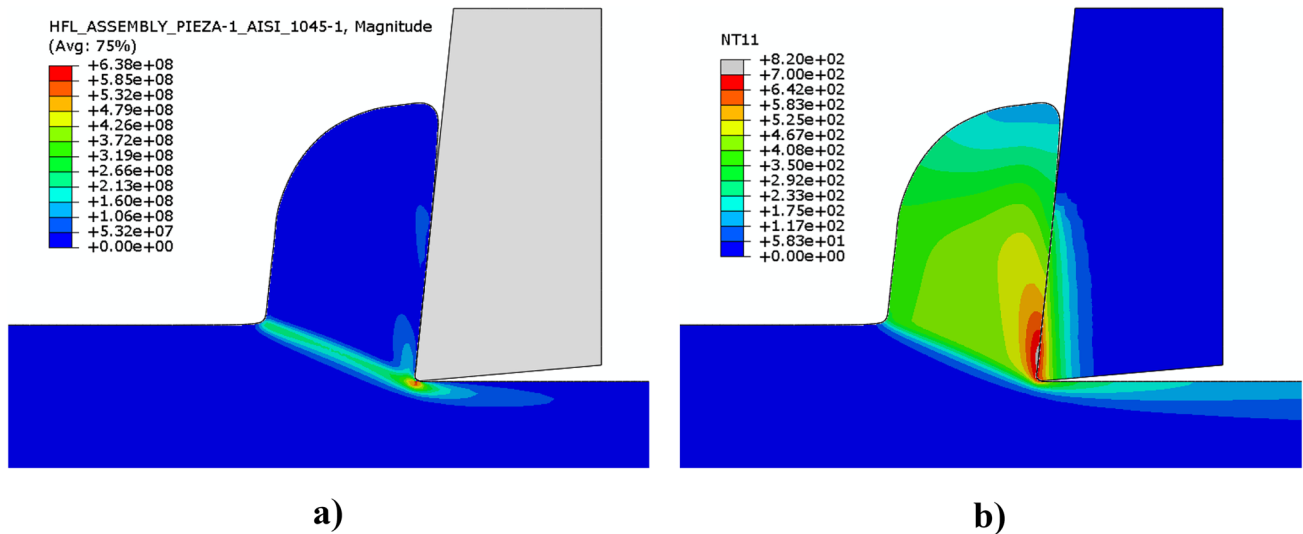
Fig. 3 **a** Heat flow during cutting for model 1 W/m^2 and **b** tool temperature field.

It was assumed that 90% of strain energy transforms into heat [28, 29]. The tool was modeled as a non-deformable solid, and its thermal properties are presented in Table 5.

A temperature-displacement explicit dynamic analysis was performed within a period of 0.0012 s due to a cut-off distance of 3 mm at 2.5 m/s speed applied in the tool reference point. A standard Coulomb friction model was used to simulate the contact effects at the tool-workpiece interaction [26]. Conductance was defined as a function of contact pressure, when pressure is zero, $k=0$; when contact pressure is greater than zero, k increases considerably; this is to simulate perfect contact at the workpiece and the tool interface and to allow a faster increase in tool temperature

[4], $k = 6E6[W/m^2 \,°C]$ was proposed. The workpiece and cutting tool's initial temperature was 20 °C.

The workpiece was modeled considering linear Eulerian hexahedral elements with 8 nodes thermally coupled (EC3D8RT); mesh size was 0.02 mm in the X and Y directions (thick mesh) for model 1 and model 3; one 2-mm-length element in the Z-direction was considered. For model 2 and model 4, a 0.01-mm-size mesh was used in X and Y directions. The mesh size variation was considered to observe correlation with chip geometric exactitude and computational time. The cutting tool considered linear Lagrangian hexahedral elements with 8 nodes thermally coupled C3D8RT, mesh size at the attacking surface increases from
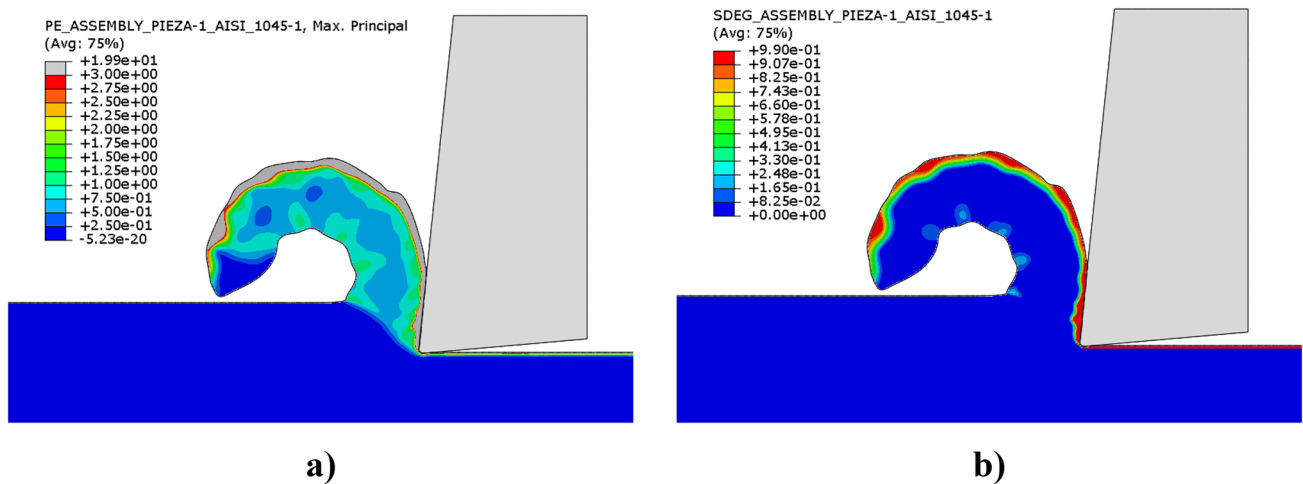

Fig. 4 Chip formation (model 2); **a** plastic strain and **b** SDEG (stress degradation)

0.001 to 0.01.4 mm as it moves away from the tip, and from 0.001 to 0.02 mm to incidence surface.

3 Results and discussion

Plastic strain distribution for model 1, presented in Fig. 2a, shows a shear zone with values around 1.5 mm/mm, and a homogeneous plastic strain distribution along the chip, showing higher values on the contact region. A residual strain can be observed on the cutting surface, resulting in an increase of strength in this region. Figure 2b shows Von Mises stress distribution for model 1. The highest value was achieved in the shear zone, reaching 1.1 GPa; this indicates that material failure will occur either in the primary shear zone, or the material-tool contact zone. Since model 1 considers a non-failure criterion, even if stress values reach failure levels, the material fracture will not occur. Contact pressure obtained along the cutting process (Fig. 2c) allows observing the contact area on the tool face increases as the cutting process begins; however, the latest stages of the process remain still, indicating the secondary shear zone and the place where the chip separation starts.
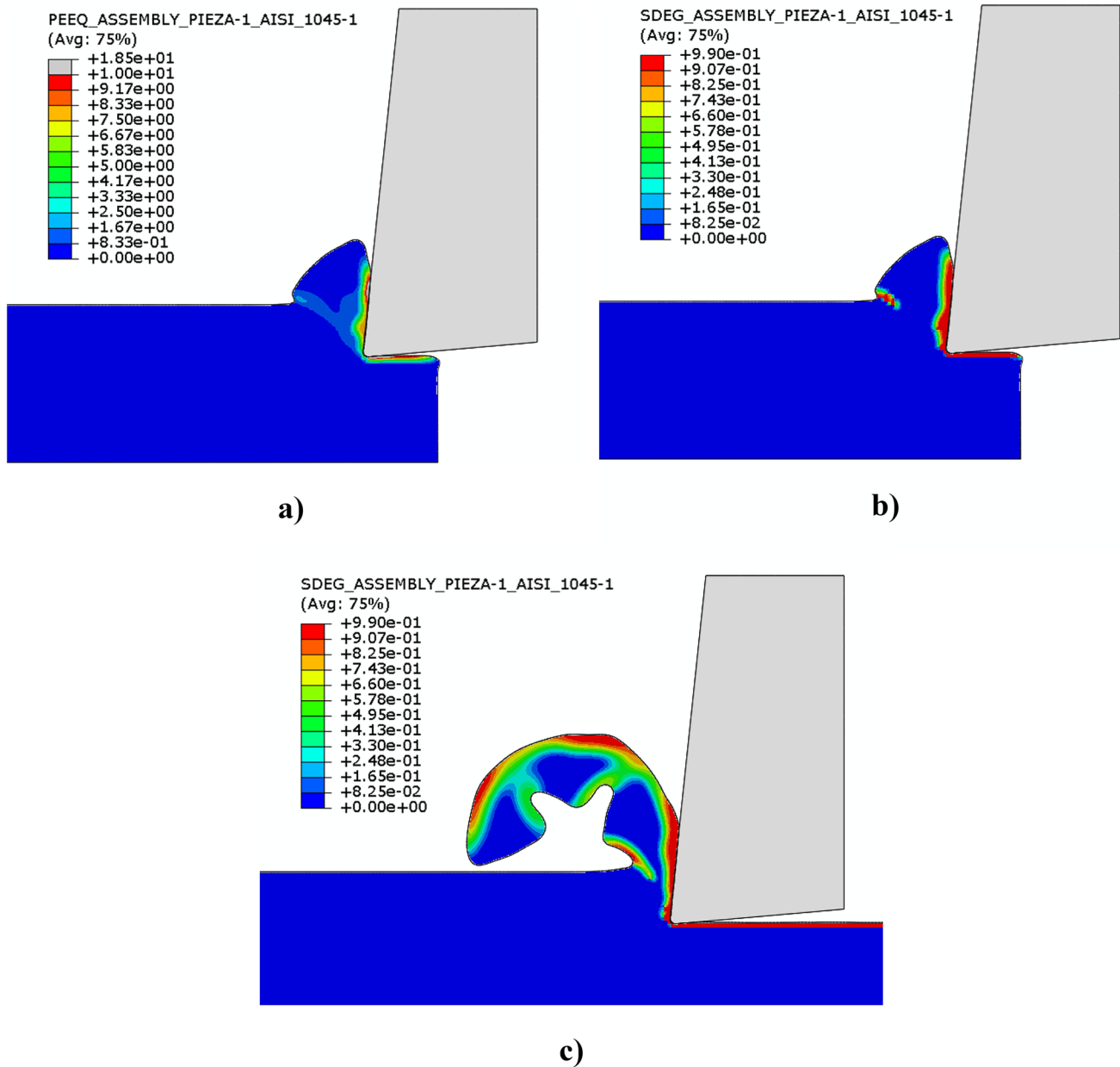

Fig. 5 Initiation of the segmented chip formation (model 3); **a** plastic strain, **b** damage variable and, **c** damage variable for segmented chip
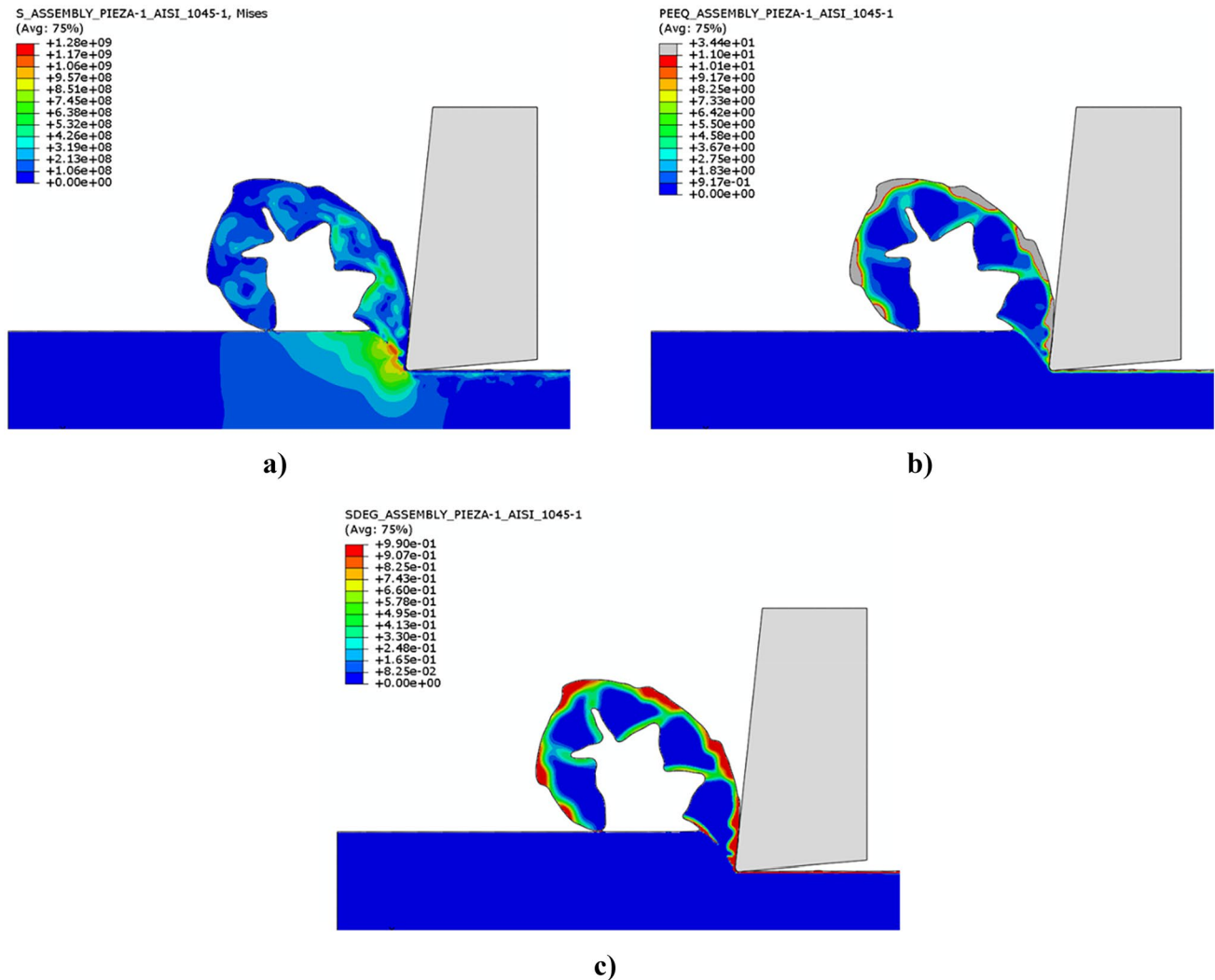
Fig. 6 Results of model 4 **a** VM stresses, **b** equivalent plastic strains, and **c** SDEG numerical simulation

Figure 3a shows the heat flow; the highest value is at the primary shear zone due to heat generated during material deformation. Figure 3b shows that the calculated temperature distribution was close to the experimental temperature distribution obtained by Artozoul et al. [21] with a relative error of about 11.2%; the highest temperature value is on the tool cutting edge and the attacking surface; this region corresponds to secondary shear zone in the workpiece, where temperature increase is produced by sliding. Tool temperature field reveals that values in inner regions were found to be lower; this can be produced by tool speed, which reduces time and limits heat transfer. Numerical simulation time is very short, hence, there is not enough time to allow heat transfer in comparison with experimental cutting results, where the maximum temperature region spreads along the tool.

The Johnson–Cook parameters considered in model 2 generated a continuous chip, shown in Fig. 4. Equivalent strain distribution (Fig. 4a) allows identifying shear band formation, while stress degradation (SDEG) values (Fig. 4b) indicate chip segmentation beginning; however, chip fracture does not continue through.

For model 3, failure criterion effects can be observed in Fig. 5, plastic strain distribution does not extend homogeneously along chip geometry, instead, concentrating on primary and secondary shear zones. Surface hardening on cut length can be also identified. The SDEG variable, shown in Fig. 5b, indicates global damage value D. Primary shear zone indicates that chip segmentation has started due to SDEG values reaching 1; chip fracture runs from the material's upper surface to the tool cutting surface, along the shear plane.

The secondary shear zone shows that material failure occurs at the chip and tool interface when deformation is generated due to friction between the tool and the material

Fig. 7 Cutting forces
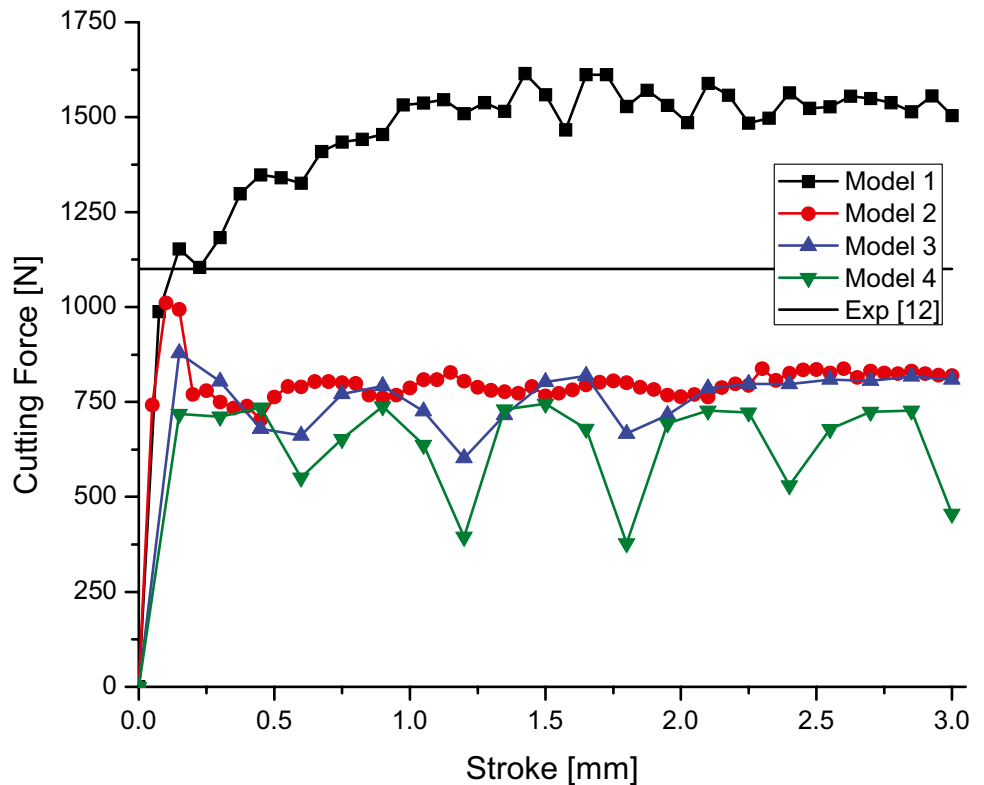
flow in the vicinity of the cutting surface. Damage criterion inclusion in model 3 led to a characteristic wavy chip morphology presented in Fig. 5c. This sinusoidal variation in thickness is usually related to low cutting speed or machine vibrations; experimental variables are considered fixed.

The Von Mises stress fields and equivalent plastic strain distribution for model 4 are shown in Fig. 6a and b, respectively. The highest stress values appear in the primary and secondary zone of deformation with values around 1.1 GPa before failure. In the secondary zone of deformation, the material fails, and stress decreases up to zero due to the failure evolution definition.

Equivalent plastic strain distribution matches with damage values (SDEG) presented in Fig. 6c, reaching in both cases the highest values over the cutting surface and secondary shear zone; this is, the damage criterion prevents plastic deformation to spread along chip surface as it occurred with no criterion damage. This sawtooth-like chip has been obtained from different experimental studies, for different materials and cutting conditions [3, 12]. Model 4 was the best, showing periodically serrated chip flow.

A higher $\bar{u}^{pl}$ value is related to thickness variation and chip morphology; low $\bar{u}^{pl}$ values allow sawtooth-like chip, as this value increases morphology tends to a wavy chip with lower thickness variation up to a continuous chip, where shear bands can be identified; but as damage values remain under 0.4, chip segmentation was not reached.

Cutting forces computed from different models and experimental cutting forces obtained by Artozoul et al. [21] are summarized in Fig. 7. Model 1 exhibits a continuous increase in cutting force up to 1 mm of tool stroke; after that, cutting force values remain still around 1540 N; no failure criterion generates a continuous chip that increases contact length, when the maximum contact length is reached, also is cutting force values.

Table 5 Tool properties [21]

Density Kg/m^3	Thermal conductivity W/mK	Thermal capacity J/KgK
11,100	37.7	276

Table 6 Comparison between experimental results and numerical models

	F_c [N]	Relative error [%]	F_c max [N]	Relative error [%]
Experimental [12]	1100	---		
Model 1	1539.9	39.99	1666.3	51.48
Model 2	800.1	27.26	1010.6	8.1
Model 3	762.6	30.66	878.8	20.1
Model 4	646.4	41.23	745.1	32.2

Table 7 Computational time for each model

Model	Time [h]
1	8.1
2	78
3	8.3
4	64

Models 2, 3, and 4 present similar behavior; cutting forces increase up to a maximum value where the onset of a new adiabatic shear band (ASB) is accompanied by a pronounced load applied to the cutting tool material separation initiates; after that, cutting forces decrease, and an oscillation around an average value can be identified. Cutting forces during material separation depend on the failure criterion value; as $\bar{u}^{\mathrm{pl}}$ values increases, the maximum value is reached, and the dropping magnitude rises. The oscillation amplitude around the average cutting value and the time in which it diminishes increase as $\bar{u}^{\mathrm{pl}}$ decreases. Every cutting force drop corresponds to a completely formed ASB [12]. Higher oscillation amplitudes are related to chip segmentation and thickness variation, as big is chip segmentation; the difference between the maximum and minimal force variation increases. Average cutting forces depend on $\bar{u}^{\mathrm{pl}}$ values, being necessary for a higher force to the continue cutting process as $\bar{u}^{\mathrm{pl}}$ value increases.

Models with damage criteria underestimate experimental cutting forces as shown in Table 6. Model 1 overestimated cutting forces due to no failure criterion used; models 3 and 4 showed higher relative error among models with damage criterion, presenting 30.66% and 41.23%, respectively, for average cutting force due to the lower values of $\bar{u}^{\mathrm{pl}}$.

The cutting force from model 2 reaches a maximum value of 1010.6 N, representing the lowest relative error obtained, 8.1%. However, the average value decreases up to 800.1 N, with a relative error of 27.26%. Then higher $\bar{u}^{\mathrm{pl}}$ values represent less error percentage.

Table 7 shows the computational time for each model; model 4 is almost 8 times longer than model 1 and model 2 and is almost 10 times longer. These times are comparable to purely Lagrangian models that reported 8 h for a simple model and 130 h for a complex model [30].

4 Conclusions

The study in this paper demonstrates the ability of the CEL method to model cutting processes and phenomena that involve material separation; it also shows that the value of the experimental forces and temperature is within the range of the values obtained in the models developed.

The minimum relative error to force Fc was 27.6% (model 2), and for maximum force Fc, it was 8.1%. Errors can be minimized by introducing more complex models to simulate the failure evolution so that it will postpone the moment, and the stress value of the material is modified after the failure, which affects the contact length and shearing forces.

Under an equivalent plastic displacement variation and failure evolution parameters, it was simulated segmented and continuous chip formation, presenting the cutting plane and bands of cutting, as well as the formation of the segments (saw-tooth) characteristic of a segmented chip.

Coupled thermo-mechanical cutting process modeling was successfully achieved since the model 1 temperature fields presented values approximate to the experimental with a relative error of 11.2%.

Availability of data and material Not applicable.

Code availability Not applicable.

Declarations

Ethics approval Not applicable.

Consent to participate Not applicable.

Consent for publication Not applicable.

Competing interests The authors declare no competing interests.

References

1. Özel T, Davim P (2009) Intelligent machining : modeling and optimization of the machining processes and systems. Wiley
2. Maranhão C, Paulo Davim J (2010) Finite element modelling of machining of AISI 316 steel: numerical simulation and experimental validation. Simul Model Pract Theory 18:139–156. https://doi.org/10.1016/j.simpat.2009.10.001
3. Ye GG, Chen Y, Xue SF, Dai LH (2014) Critical cutting speed for onset of serrated chip flow in high speed machining. Int J Mach Tools Manuf 86:18–33. https://doi.org/10.1016/j.ijmachtools.2014.06.006
4. Sima M, Özel T (2010) Modified material constitutive models for serrated chip formation simulations and experimental validation in machining of titanium alloy Ti–6Al–4V. Int J Mach Tools Manuf 50:943–960. https://doi.org/10.1016/j.ijmachtools.2010.08.004
5. Umbrello D (2008) Finite element simulation of conventional and high speed machining of Ti6Al4V alloy. J Mater Process Technol 196:79–87. https://doi.org/10.1016/j.jmatprotec.2007.05.007
6. Braess H, Wriggers P (2000) Arbitrary Lagrangian Eulerian finite element analysis of free surface flow. Comput Methods Appl

Mech Eng 190:95–109. https://doi.org/10.1016/S0045-7825(99)00416-8

7. Liu C, Wan M, Yang Y (2021) Simulation of the chip morphology together with its evolution in machining of Inconel 718 by considering widely spread cutting speed. Int J Adv Manuf Technol 116:175–195. https://doi.org/10.1007/s00170-021-07346-2

8. Tang L, Huang J, Xie L (2011) Finite element modeling and simulation in dry hard orthogonal cutting AISI D2 tool steel with CBN cutting tool. Int J Adv Manuf Technol 53:1167–1181. https://doi.org/10.1007/s00170-010-2901-2

9. Cai Q-Q, Xu J-K, Yu Z-J et al (2021) Numerical and experimental study on orthogonal cutting of GH4169 superalloy by micro-pit textured cutter BT - Mechanical Engineering and Materials. In: Pandey KM (ed) Xu J. Springer International Publishing, Cham, pp 133–142

10. Miller L, Zhou K, Tang J et al (2021) Thermomechanical finite element simulation and correlation analysis for orthogonal cutting of normalized AISI 9310 steels. Int J Adv Manuf Technol 114:3337–3356. https://doi.org/10.1007/s00170-021-07130-2

11. Xu D, Feng P, Li W et al (2014) Research on chip formation parameters of aluminum alloy 6061–T6 based on high-speed orthogonal cutting model. Int J Adv Manuf Technol 72:955–962. https://doi.org/10.1007/s00170-014-5700-3

12. Yaich M, Ayed Y, Bouaziz Z, Germain G (2017) Numerical analysis of constitutive coefficients effects on FE simulation of the 2D orthogonal cutting process: application to the Ti6Al4V. Int J Adv Manuf Technol 93:283–303. https://doi.org/10.1007/s00170-016-8934-4

13. Khoei AR, Anahid M, Shahim K (2007) An eXtended Arbitrary Lagrangian-Eulerian finite element model (X-ALE-FEM) in large plasticity deformations. In: AIP Conference Proceedings. AIP 1495–1500

14. Khoei AR, Anahid M, Shahim K (2007) An extended arbitrary Lagrangian–Eulerian finite element modeling (X-ALE–FEM) in powder forming processes. J Mater Process Technol 187–188:397–401. https://doi.org/10.1016/j.jmatprotec.2006.11.137

15. Khoei AR, Anahid M, Shahim K (2008) An extended arbitrary Lagrangian–Eulerian finite element method for large deformation of solid mechanics. Finite Elem Anal Des 44:401–416. https://doi.org/10.1016/j.finel.2007.12.005

16. Malakizadi A, Hosseinkhani K, Mariano E et al (2017) Influence of friction models on FE simulation results of orthogonal cutting process. Int J Adv Manuf Technol 88:3217–3232. https://doi.org/10.1007/s00170-016-9023-4

17. Qiu G, Henke S, Grabe J (2011) Application of a coupled Eulerian–Lagrangian approach on geomechanical problems involving large deformations. Comput Geotech 38:30–39. https://doi.org/10.1016/j.compgeo.2010.09.002

18. Ducobu F, Rivière-Lorphèvre E, Filippi E (2016) Application of the coupled Eulerian-Lagrangian (CEL) method to the modeling of orthogonal cutting. Eur J Mech - A/Solids 59:58–66. https://doi.org/10.1016/j.euromechsol.2016.03.008

19. Ducobu F, Arrazola P-J, Rivière-Lorphèvre E et al (2017) The CEL method as an alternative to the current modelling approaches for Ti6Al4V orthogonal cutting simulation. Procedia CIRP 58:245–250. https://doi.org/10.1016/j.procir.2017.03.188

20. Ducobu F, Rivière-Lorphèvre E, Galindo-Fernandez M, et al (2019) Coupled Eulerian-Lagrangian (CEL) simulation for modelling of chip formation in AA2024-T3. Procedia CIRP 82:142–147. https://doi.org/10.1016/j.procir.2019.04.071

21. Artozoul J, Lescalier C, Bomont O, Dudzinski D (2014) Extended infrared thermography applied to orthogonal cutting: mechanical and thermal aspects. Appl Therm Eng 64:441–452. https://doi.org/10.1016/j.applthermaleng.2013.12.057

22. Özel T, Zeren E (2005) Finite element method simulation of machining of AISI 1045 Steel With A Round Edge Cutting Tool. Proceedings of 8th CIRP International Workshop on Modeling of Machining Operations, Chemnitz, Germany May 10-11, 2005: pp 533-542

23. Johnson GR, Cook WH (1983) A constitutive model and data for metals subjected to large strains, high strain rates, and high temperatures. In: Proceedings 7th International Symposium on Ballistics. pp 541–547

24. Davies MA, Cao Q, Cooks AL, Ivester R (2003) On the measurement and prediction of temperature fields In machining AISI 1045 steel. CIRP Ann 52:77–80. https://doi.org/10.1016/S0007-8506(07)60535-6

25. Duan C, Zhang L (2013) A reliable method for predicting serrated chip formation in high-speed cutting: analysis and experimental verification. Int J Adv Manuf Technol 64:1587–1597. https://doi.org/10.1007/s00170-012-4125-0

26. ABAQUS Inc. (2012) ABAQUS 6.12 Analysis User's Manual

27. Vaziri MR, Salimi M, Mashayekhi M (2010) A new calibration method for ductile fracture models as chip separation criteria in machining. Simul Model Pract Theory 18:1286–1296. https://doi.org/10.1016/j.simpat.2010.05.003

28. Ducobu F, Rivière-Lorphèvre E, Filippi E (2014) Numerical contribution to the comprehension of saw-toothed Ti6Al4V chip formation in orthogonal cutting. Int J Mech Sci 81:77–87. https://doi.org/10.1016/j.ijmecsci.2014.02.017

29. Iskra P, Tanaka C, Ohtani T (2005) Energy balance of the orthogonal cutting process. Holz als Roh- und Werkst 63:358–364. https://doi.org/10.1007/s00107-005-0021-8

30. Kalhori V (2001) Modelling and simulation of mechanical cutting. Lulea University of Technology